

***Ab initio* data-analytics study of carbon-dioxide activation on semiconductor oxide surfaces**

A. Mazheika¹, Y. Wang¹, R. Valero², L. M. Ghiringhelli¹, F. Viñes,² F. Illas², S. V. Levchenko^{3,1}, M. Scheffler¹

¹Fritz-Haber-Institut der Max-Planck-Gesellschaft, 14195 Berlin-Dahlem, Germany

²Departament de Ciència de Materials i Química Física and

Institut de Química Teòrica i Computacional (IQTUB),

Universitat de Barcelona, Martí i Franquès 1, Barcelona 08028, Spain

³Skolkovo Institute of Science and Technology, Skolkovo Innovation Center,

3 Nobel Street, 143026 Moscow, Russia

Abstract

The excessive emissions of carbon dioxide (CO₂) into the atmosphere threaten to shift the CO₂ cycle planet-wide and induce unpredictable climate changes. Using artificial intelligence (AI) trained on high-throughput first principles based data for a broad family of oxides, we develop a strategy for a rational design of catalytic materials for converting CO₂ to fuels and other useful chemicals. We demonstrate that an electron transfer to the π^* -antibonding orbital of the adsorbed molecule and the associated bending of the initially linear molecule, previously proposed as the indicator of activation, are insufficient to account for the good catalytic performance of experimentally characterized oxide surfaces. Instead, our AI model identifies the common feature of these surfaces in the binding of a molecular O atom to a surface cation, which results in a strong elongation and therefore weakening of one molecular C-O bond. This finding suggests using the C-O bond elongation as an indicator of CO₂ activation. Based on these findings, we propose a set of new promising oxide-based catalysts for CO₂ conversion, and a recipe to find more.

Introduction

The need for converting stable molecules such as carbon dioxide (CO₂), methane, or water into useful chemicals and fuels is growing quickly along with the depletion of fossil-fuel reserves and the pollution of the environment ^{1,2}. Such a conversion presents a great challenge that does not have a satisfactory solution so far. The challenge lies in breaking the strong chemical bonds within these very stable molecules and simultaneously ensuring that the useful products as well as the surface catalytic activity are preserved under the same conditions. For example, the strong C-O double bonds in CO₂ can be weakened or even broken by adsorption at a solid surface at an elevated temperature, but this usually also implies a strong adsorption or further dissociation of the molecule, so that the catalytic surface is poisoned by carbonate or carbon deposits.

The intuitive understanding that a stable molecule needs to be “prepared”, before its catalytic conversion occurs, leads to the notion of molecular activation, which is often used in heterogeneous catalysis ³. However, on one hand, this notion encompasses a very wide variety of processes (adsorption, photo-excitation, application of electric field, etc.) and materials (including compositional and structural variability, e.g., extended surfaces versus supported nanoparticles), and it remains unclear which properties of the catalytic material and the adsorbed molecule determine the final chemistry, what is the relationship between the two sets of properties, and how general this relationship may be. On the other hand, finding descriptors/features of a catalytic material that can be quantitatively related to its catalytic performance in a particular process, or even in general for a given reactant, would be very valuable, because it would allow us to quickly search for promising candidate catalysts using rational design ⁴. One way to find such descriptors for a given reaction is to explore the potential-energy surface for each catalyst candidate, a slow and time-consuming process. However, a reliable calculation of turn-over-frequencies (TOF), selectivity, and yields at realistic conditions for many materials on a high-throughput basis is, as already mentioned, currently computationally unfeasible. An alternative approach consists in searching for a correlation between experimentally determined material’s properties and its catalytic performance. However, for such a strategy to work at all, consistent experimental measurements at well-defined conditions for a set of materials are required. To our knowledge, such data have not been reported so far for challenging reactions such as CO₂ conversion.

Yet another strategy is to find an *indicator* of activation, namely, a property of the system that correlates with catalytic performance of the material ⁴. We distinguish here indicator from descriptors based on a qualitatively different level of computational complexity. The indicator can still be unfeasible or hard for a high-throughput study of hundreds of thousands or millions of materials. However, if it can be calculated for a few tens or hundreds of materials in a reasonable

time, these data could then be used to find a descriptor which is much easier to evaluate. Since a direct search for a relationship between the indicator and catalytic performance of a material would also require a consistent set of data of TOF, selectivity, and yield values, one could instead consider a few most promising indicators, find out which materials are predicted to be good catalysts according to each indicator, and then check whether these materials are known as good catalysts. This approach also addresses the problem of defining activation in terms of the adsorbed-molecule properties.

In this work, we adopt the latter strategy. We focus on the CO₂ conversion as one of the most important societal and technological challenges^{1,2,5,6,7,8}, and oxide materials as candidate catalysts. Oxides are structurally and compositionally stable under realistic temperatures and can be less expensive than the traditional precious metal containing catalysts. Furthermore, we consider only semiconducting (or insulating) oxides, and do not consider defects (e.g., oxygen vacancies) and charge-carrier doping, which can significantly modify surface chemical properties^{9,10,11}. Despite these constraints, the selected materials class includes a huge number of compounds (binary, ternary, and more complex oxides), and the overall approach, which combines first principles calculations and artificial-intelligence (AI) training and predictions, is applicable to a wider class of materials and molecules, not limited to oxides or CO₂. Our study by no means encompasses all possible mechanisms of CO₂ conversion on oxide surfaces, but offers a clear design path among many possible ones. Our analysis should be considered *complementary* to the analysis of a material's suitability for a particular application in terms of stability at reaction conditions and other characteristics¹². The methodology used in this work is novel among other data-analytics approaches ever used in computational heterogeneous catalysis¹³.

Computational details

The calculations are performed using density-functional theory (DFT) with the PBEsol functional¹⁴. The functional is chosen based on a comparison of calculated bulk lattice constants¹⁴ and CO₂ adsorption energy to the available experimental results and high-level calculations (see Supporting Information (SI) for more details on the computational setup). Nevertheless, it is expected that, because of the large set of systems inspected and the small variations introduced by the functional choice, the main trends will hold even when using another functional.

The data set includes 71 semiconductor oxide materials, with about two surface cuts per material (141 surfaces). The materials are ternary (ABO_3) and binary oxides with metal cations A and B from groups 1 to 5 (including La) and groups 12 to 15 of the periodic table. The full list of materials and surface cuts is given in SI. In this study we considered only surface reconstructions obtained by atomic relaxation of stoichiometric bulk-like initial surface geometries. While this is

certainly a limitation, our results show that indicators of activation calculated with this assumption correlate with experimental activity for known good oxide catalysts. This does not imply that surfaces of these materials do not reconstruct under catalytic conditions, but that (possibly) reconstructed surfaces inherit important features of the unreconstructed ones. Surface defects and reconstructions can drastically change catalytic activity under realistic conditions, and will be a subject of future work on different design paths.

We find that on semiconductor oxide surfaces CO_2 is activated exclusively when the carbon atom binds to surface O-atoms. All other minima of the potential-energy surface are found to be either metastable or correspond to physisorption. Therefore, there are as many different potential chemisorption sites as there are unique O atoms at the surface. The data set includes all non-equivalent O atoms on the considered surfaces, which sum up to 270 unique adsorption sites. Among these sites on about 9% (23 out of 270) CO_2 prefers to physisorb, i.e., any chemisorbed state at these sites is metastable with respect to the physisorbed one. The physisorption can be easily identified by an almost linear geometry of the adsorbed molecule, and a C-O bond distance very close to the C-O bond length in a gas-phase CO_2 molecule, 1.17 Å. These sites are excluded from the data set prior to analysis, so that AI is focused directly on activated CO_2 . Results for the data set including both chemisorption and physisorption cases are given in the SI.

We considered several possible candidate indicators of CO_2 activation. Bending of the OCO angle in the adsorbed CO_2 molecule relative to the gas-phase value of 180° (linear configuration) has been previously proposed¹⁵ and widely accepted as a good indicator of activation. The C-O double bond is weakened when an electron is added to the lowest unoccupied orbital, because it is of antibonding (π^*) character. For a gas-phase CO_2 , this also causes bending of the molecule. There is a one-to-one mapping between the C-O bond length $l(\text{C-O})$ and the OCO angle in $\text{CO}_2^{\delta-}$ for a range of $\delta > 0$ (red curve in Fig. 1). However, this is not the case for the adsorbed CO_2 (black symbols in Fig. 1). There is a subset of adsorption sites for which the correlation between $l(\text{C-O})$ (larger of the two C-O bond lengths in the case of asymmetric structures) and the OCO angle holds, but there are also many adsorption sites where $l(\text{C-O})$ is substantially larger for a given OCO angle. A longer C-O bond implies its weakness and readiness for further chemical transformations. Thus, the bond elongation itself may be a better indicator of activation than just focusing on the bending. A quick look at the adsorbed CO_2 structures reveals that, on sites following the gas-phase correlation, the molecule adsorbs in such a way that the distance between O-atoms of CO_2 and neighborhood surface atoms is about the same, resulting in nearly equal length of the two C-O bonds. In the case of the outliers, where only one O atom of CO_2 is approaching surface cations, the asymmetry of the adsorbed molecule is much more pronounced.

We have also considered other potential indicators of activation, namely Hirshfeld charge¹⁶ of adsorbed CO₂ (a direct indicator of the charge transferred to CO₂), dipole moment of the surface slab model along the surface normal per adsorbed CO₂ molecule (includes charge rearrangement not only due to charge transfer to the molecule, but also atomic relaxation around adsorbed CO₂), the difference in Hirshfeld charges of C and O atoms in an adsorbed CO₂ molecule (indicates the ionicity of C-O bonds), and the difference in Hirshfeld charges of the O atoms in the adsorbed molecule (indicates asymmetry of the adsorbed molecule).

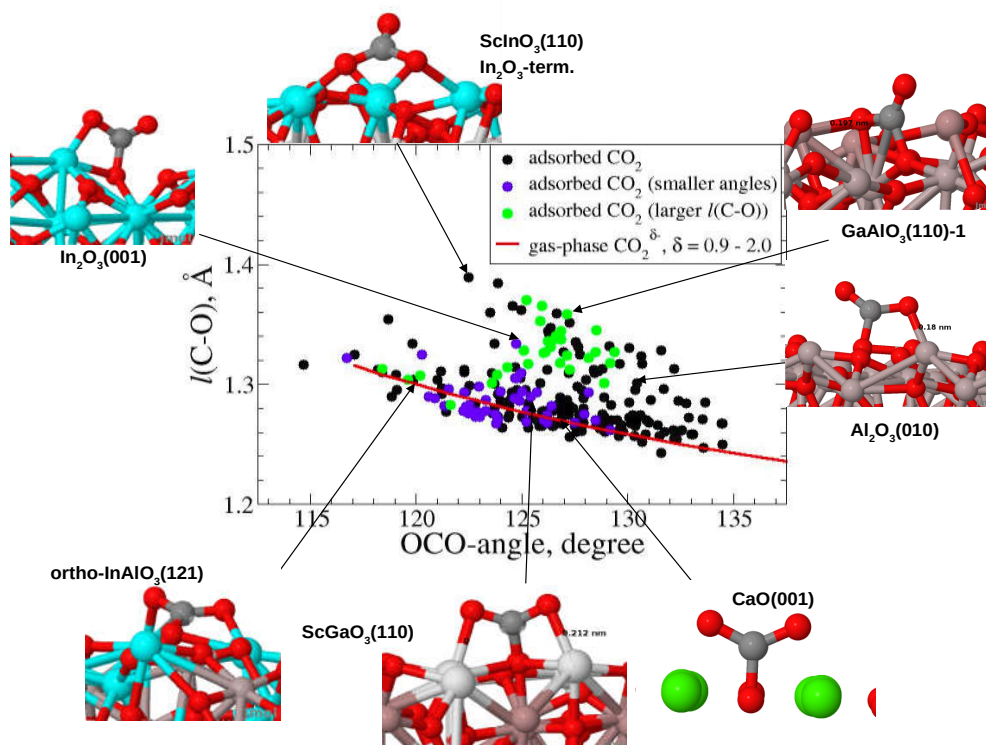


Figure 1. The correlation between the larger of the two C-O bond lengths (in case the two bond lengths are different) and the OCO-angle in charged gas-phase (red line) and adsorbed CO₂ (dots). Colored dots: blue – adsorption sites from the subgroup with smaller OCO-angles, green – subgroup with larger $l(\text{C-O})$, black – the remaining samples (see the text).

As discussed above, for physical reasons the above indicators are expected to be either minimized (OCO angle, dipole moment, negative Hirshfeld charge¹⁶ of adsorbed CO₂) or maximized (the rest) for a good catalyst. To find out which properties (features) of the clean surfaces determine when a given activation indicator is maximized or minimized, we employ a recently developed subgroup-discovery (SGD) approach^{17,18}. Given a dataset and a target property known for all data points, the SGD algorithm identifies subgroups with “outstanding characteristics” (see further) and describes them by means of selectors (statements) of the kind (feature1 < x) AND (feature2 ≥ y) AND

To be practically useful, the selectors should only contain features that are much easier to evaluate than the target property. The considered features include properties of gas-phase atoms of the types that are present at the surface, gas-phase CO₂, and collective properties related to the pristine material (properties of the bulk phase of the stoichiometric solid, of the pristine surface, and site-specific features). Overall 51 primary features have been considered. The full list is presented in SI. The features selected by the SGD are summarized in Table 1.

Table 1. A shortlist of features used in this work according to PBEsol.

symbol	Meaning
M	energy at which the O $2p$ -band projected density of states (PDOS) is maximal
d_1, d_2, d_3	distances from surface O-atom to the first-, second-, and third-nearest cations
W	work function W , as the negative of the valence band maximum ($W = -VBM$)
q_{\min}, q_{\max}	minimal and maximal Hirshfeld charges of cations in the pair A and B , calculated as an average for all surface cations of a given type
Δ^{bulk}	band gap of the bulk material
$IP_{\min/\max}, IP_{\text{O}}$	ionization potential, minimal and maximal in the pair of atoms A and B , and for O; calculated as $E_{\text{atom}} - E_{\text{cation}}$
$EA_{\min/\max}, EA_{\text{O}}$	electron affinity, minimal and maximal in the pair of atoms A and B , and for O; calculated as $E_{\text{anion}} - E_{\text{atom}}$
$EN_{\min/\max}$	Mulliken electronegativity, minimal and maximal in the pair of gas-phase atoms A and B
d_2^{unrelax}	distance from O-atom to the second-nearest cation on an unrelaxed surface cut
$r_{\min/\max}^{\text{HOM}}$ O-1	radii of the maximum value of radial wave functions of the spin-unpolarized spherically symmetric atom for HOMO-1, maximum (max) and minimum (min) in the pair of atoms A and B
$r_{\min/\max}^{\text{LUMO}}$	radii of the maximum value of radial wave functions of the spin-unpolarized spherically symmetric atom for LUMO, maximum (max) and minimum (min) in the pair of atoms A and B
$q_{\min/\max}^{\text{bulk}}$	minimal and maximal Hirshfeld charges of bulk material cations in the pair A and B , calculated as an average for all surface cations of a given type
$\alpha_{\min}, \alpha_{\max}, C_6^{\min}, C_6^{\max}$	polarizability and C_6 -coefficient for cations, minimal and maximal in the pair A and B , calculated as an average for all surface cations of a given type
q_{O}	Hirshfeld charge of O-atom
wid_{\min}, wid_{\max}	square root of the second moment of PDOS of cations within valence band, minimal and maximal in the pair A and B , calculated as an average for all surface cations of a given type
VBM	valence-band maximum with respect to vacuum level
E_{form}	surface formation energy
L_{\min}, L_{\max}	energy of lowest unoccupied state of cation, minimal and maximal in the pair A and B , calculated as an average for all surface cations of a given type

The outstanding subgroup should satisfy several requirements: it does not have to be too small in order to avoid the identification of small subgroups with little statistical significance; the distribution of the data has to be rather narrow which would mean that these data points have something in common; the average or median value of a subgroup should deviate from the same value for the whole sampling as much as possible in a given direction since we are interested in the subgroups with large or small values of a target property. Following ¹⁷, we employ a quality function:

$$F(Z) = \frac{s(Z)}{s(Y)} \left(\frac{med(Z) - med(Y)}{mm(Y) - med(Y)} \right) \left(1 - \frac{amd(Z)}{amd(Y)} \right) \quad (1)$$

where Y is the whole data set, Z – a subgroup, s - sampling size, med - median of the target property, mm – minimal or maximal value of the target property in the whole sampling, amd - absolute median deviation calculated around the median value of the target property. The search of subgroups is performed using an iterative Monte Carlo (MC) scheme ¹⁸. In our work, the features used to construct the selectors for SGD are primary features shown in Table S4 in SI excluding features that are constant for all materials (CO₂ molecule and O atom properties), overall leading to 46 features. The cut-off values x, y, \dots are obtained by k -means clustering. That is, for a desired number $n = k - 1$ of cut-off values a set of k representative values of a given feature and k groups (clusters) of the data points are determined that minimize the deviation of all the feature values from the representative values. Thus, each value of the feature in the data set is assigned to a particular cluster, and the cut-offs are determined as the arithmetic mean between the closest feature values in neighboring clusters. The number k is a parameter, and different k -values can in principle result in different cut-off values. It is worth noting that, due to the stochastic MC sampling, the exact definitions of the subgroups may vary for consecutive runs of the SGD algorithm. We have tested $k = 12, 14,$ and 16 and rerun the algorithm several times for each k . While the results indeed depend on the run and on the k value, the subgroups maximizing the quality function have similar extensions and selectors. Below, we report selectors that appear most often and have a high extension and quality function values.

We note that SGD is qualitatively different from standard classification/regression techniques such as neural networks, kernel regression methods, or tree regression (e.g., random forest). The standard approaches require that each data point is pre-labelled as belonging or not to the subgroup. On the contrary, SGD identifies the subgroups in an unsupervised manner. It directly identifies common features of materials that optimize the utility function, without constructing an explicit model for the target property.

Results of the subgroup discovery

The physical motivation for considering $l(\text{C-O})$ as an indicator of CO_2 activation is that longer C-O bonds are weaker, which implies that it would be easier for the molecule to undergo further chemical transformations. In order to obtain the subgroups of adsorption sites with larger $l(\text{C-O})$, we performed the SGD with $mm = \max$ in the quality function (1) and $l(\text{C-O})$ as target property. One of the best-found selectors is $(q_{\min} < 0.48 e)$ AND $(W > 5.18 \text{ eV})$ AND $(d_2 > 2.14 \text{ \AA})$. This corresponding subgroup contains 30 sites, including 19 sites on surfaces of $A^{1+}B^{5+}\text{O}_3$ ($A = \text{Li, Na, K, Rb, Cs}$; $B = \text{Nb, Sb, V}$) materials, and the rest on $A^{3+}B^{3+}\text{O}_3$ (A and $B = \text{Al, Ga, In, La, Sc, Y}$) materials. The median $l(\text{C-O})$ in this subgroup is 1.33 \AA and the standard deviation from the median is 0.02 \AA . In the majority of cases, in particular on $A^{1+}B^{5+}\text{O}_3$ surfaces, CO_2 molecules are adsorbed in an asymmetric position, with one O-atom of CO_2 interacting with a nearby cation and the other one protruding. The longer C-O bond is between the carbon atom and the O atom bonded with a cation. This bond length is close to the distance between the cation and the surface O atom at which CO_2 is adsorbed and, in the vast majority of samples, is larger than 1.3 \AA . The distribution of $l(\text{C-O})$ values in the whole data set is shown in SI, Fig. S3.

The standard supervised machine-learning methods require cross-validation (CV) to find the optimal set of hyperparameters for bias-variance tradeoff. Although here we use conceptually different approach, we apply CV methods similar to the standard approaches to test predictive power of the obtained models. We performed a leave-10%-out CV to estimate how stable the subgroups are. In this method 10% samples were randomly and uniformly removed from the data set sorted according to target values, and for the rest 90% set the SGD was done. The procedure was repeated 10 times. The uniformity in removal of samples is necessary to avoid possible loss of potential subgroups, since the size of identified subgroups is usually 12-18% of the whole data set. The leave-10%-out CV showed that the same subgroup are found by SGD in 100% cases, although the value of the quality function is not always maximal. The values in selectors change in 10% cases for q_{\min} , in 70% cases for W (for up to 0.21 eV), and in 10% cases for d_2 . In 20% cases misclassified samples were obtained: in 10% two samples were incorrectly predicted to belong to a subgroup, and in other 10% cases two samples were incorrectly predicted to be outside the subgroup. Thus, the CV shows that obtained subgroup is stable.

The SGD of OCO angles was done with $mm = \min$ in eq. (1) and OCO as a target property, since smaller angles indicate larger charge transferred to the molecular π^* orbital. The SGD shows that the energy at which the O $2p$ -band PDOS (referenced to the vacuum level) is maximal, M , appears most often in the best selectors. One of these selectors is $(M > -6.0 \text{ eV})$ AND $(d_1 \geq 1.80 \text{ \AA})$ AND $(d_2 > 2.14 \text{ \AA})$. The corresponding subgroup contains 46 sites, with the median value 123.8° and standard deviation from the median 2.4° . It consists of binary oxides ($\text{CaO, SrO, BaO, La}_2\text{O}_3$

and Na₂O) and mostly those ternary oxides that are terminated with a layer of mentioned binary oxides (about 79%). On the majority of the sites in the considered subgroup CO₂ adsorbs in a symmetric configuration, with the two C-O bonds of about the same length. As discussed above, such adsorption is characteristic of systems that mostly follow the gas-phase correlation between the C-O bond length and the OCO angle. As it is shown in Fig. 1, this is the case for the majority of the sites. The overlap with the subgroup of sites with larger $l(\text{C-O})$ is only two samples.

Found subgroups do not include all samples with $l(\text{C-O}) > 1.3 \text{ \AA}$ or small OCO angles. The reason is that the SGD finds the subgroups of samples that have common quantitative features. The remaining samples with long $l(\text{C-O})$ or small OCO are unique and do not follow the general trend, or the number of outlying data points is not sufficient to form a subgroup. Other subgroups found by SGD with larger $l(\text{C-O})$ or smaller OCO significantly overlap with the ones presented here (see SI).

The subgroups found by SGD for the dipole moment induced by CO₂ adsorption, its total Hirshfeld charge, and the difference of charges on C and O atoms significantly overlap with the subgroup of smaller OCO-angles. The subgroup found by maximizing the difference of Hirshfeld charges on O-atoms of an adsorbed CO₂ largely overlaps with the subgroup of sites delivering larger $l(\text{C-O})$. Therefore, below we focus on OCO angle and $l(\text{C-O})$ as indicators of CO₂ activation. More details about the other indicators can be found in Appendix.

Analysis of the obtained subgroups

The selector for the OCO angle subgroup contains the condition $M > -6.0 \text{ eV}$, i.e., the O sites in this subgroup are easier to ionize and are therefore more ionic (basic). Thus, the smaller OCO angle correlates with the surface basicity, as expected based on the dependence of the OCO angle in the gas-phase CO₂ molecule on the charge. The comparison of the OCO angles for the “smaller angle” and “larger C-O bond” subgroups (Fig. 2, left) reveals that most of the members of the latter are on the larger-angle side of the former, but not much larger.

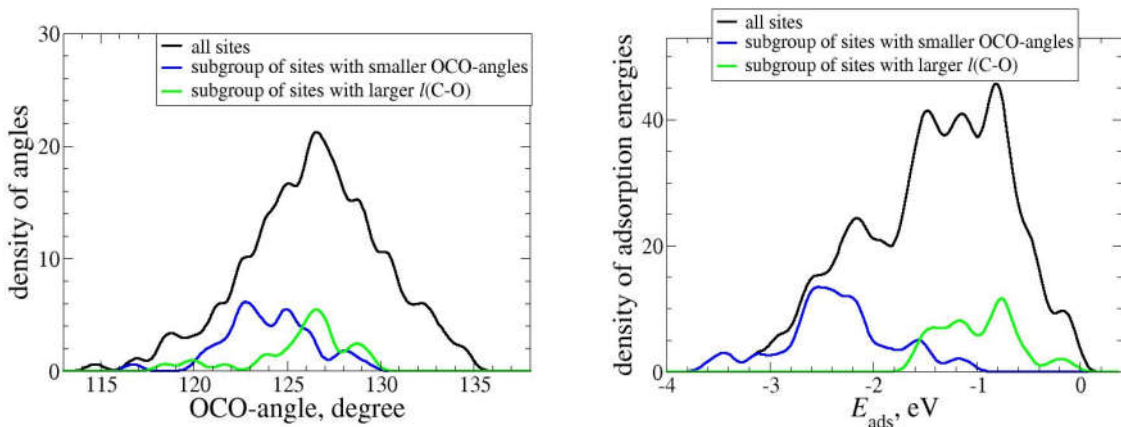


Figure 2. Distribution of OCO-angles (left) and adsorption energies (right) for the whole data set, the subgroup of sites with larger $l(\text{C-O})$ (green), and the subgroup of sites with smaller OCO angles (blue). The adsorption energy E_{ads} is defined as the difference between the total energy of the slab with adsorbed CO_2 and the sum of total energies of the clean slab and an isolated CO_2 molecule.

To address the question whether any of the discussed properties can serve as an indicator of the catalytic activity, we look closer at the members of the corresponding subgroups and check if they are active for CO_2 conversion of any kind according to the existing literature (Table 2). It should be stressed that the available experimental data are scarce and are difficult to compare quantitatively. We consider thermally- and photo-driven catalysis, and also include supported metal catalysts with the considered oxides as support. Despite possibly different mechanisms for CO_2 conversion in the different types of catalysis, properties of adsorbed CO_2 molecule can still serve as indicators of the catalytic activity. Thus, it is possible that there are common indicators of CO_2 activation. As described below, our analysis confirms this assumption.

Table 2. The catalytic performance of materials which contain the sites from larger $l(\text{C-O})$ or/and smaller OCO subgroups.

	Material	catalytic reaction
sites only from larger $l(\text{C-O})$ subgroup	LaGaO_3	cathode material in electro-chemical CO_2 reduction ²⁰
	NaNbO_3	photocatalytic CO_2 reduction with $\sim 70\%$ of CO selectivity ^{21,23}
	NaVO_3	CH_4 carboxylation with CO_2 in aqueous solutions at 25-100 °C ²⁴
	LaAlO_3	dry reforming of methane with Ni-nanoparticles; performance is higher than for Ni- La_2O_3 ²⁵

	KNbO ₃	photocatalytic reduction of CO ₂ into CH ₄ as a composite with Pt/g-C ₃ N ₄ ; significant improvement of activity when compared to Pt/g-C ₃ N ₄ ; Pt-KNbO ₃ is ~2.5 times more photoactive than Pt-NaNbO ₃ ^{21,22}
materials with sites from larger $l(\text{C-O})$ and from smaller OCO subgroups	CaTiO ₃	CO ₂ hydrogenation under UV-irradiation, although activity is not very high ^{28,31} ; twice higher activity with Ni nanoparticles ³¹
	CaZrO ₃ , SrZrO ₃ , BaZrO ₃ , SrTiO ₃	reverse water gas shift reaction (RWGS) under 700-1100°C ²⁷
	SrTiO ₃	photocatalytic CO ₂ methanation with Pt, Au-nanoparticles, significant decrease of activity during reaction ³²
sites only from smaller OCO subgroup	YInO ₃	no activity observed in photocatalytic CO ₂ conversion ¹⁹
	CaO, SrO, BaO, Na ₂ O	strong carbonation, candidate materials for carbon capture and storage (CCS) ²⁶
	La ₂ O ₃	dry reforming of methane with supported Ni-nanoparticles; lower performance than on Ni-LaAlO ₃ ²⁵ and on some other supported catalysts ²⁹ at 700 and 250°C correspondingly
	CaO	twice smaller reaction rate in CO ₂ reforming of methane reaction with supported Ni nanoparticles than on Ni-La ₂ O ₃ ³⁰ at 750°C

For the materials with the most energetically favorable site on the most stable surface belonging to the smaller OCO subgroup there are hardly any reports of successful CO₂ conversion, also when these materials are used as supports for metal nanoparticles (Table 2). This is explained by the fact that for the sites from this subgroup the absolute adsorption energies are very large, usually above 2 eV (Fig. 2, right), indicating that the surfaces of materials containing mainly these sites will be permanently poisoned by carbonate species at realistic temperatures. Therefore, these materials may be useful for CCS but do not for catalytic conversion of CO₂. According to the JANAF thermochemical tables ³³, the value of -2 eV for gas-phase CO₂ chemical potential (relative to 0 K) corresponds to a temperature of 803 K (530 °C). This means that at low, especially room, temperature hardly any reaction of CO₂ conversion can proceed on these materials. Moreover, as shown in the Table 2, even at increased temperatures, 700-750 °C, the activity of materials with sites from the smaller OCO-subgroup is low. As already mentioned, some of these materials have been considered as candidate materials for carbon capture and storage (CaO, SrO, BaO, Na₂O) ²⁶, which implies formation of stable carbonates and not CO₂ transformation.

On the other hand, *several* of the materials with larger $l(\text{C-O})$ sites are known as good materials for CO₂ conversion (Table 2) in different reactions proceeding at room or higher temperatures. For these sites, the absolute adsorption energies are lower than in the case of smaller-

OCO subgroup (Fig. 2, right), and most are higher than the chemical potential of gas phase CO₂ at the room temperature (-0.56 eV). Thus, the majority of these larger $l(\text{C-O})$ sites satisfy Sabatier principle. According to this principle, a good catalyst should bind the reactants strongly enough to fix them on the surface, but weakly enough so that it can be restored in the course of the catalytic reaction. Interestingly, some of the materials with sites in the larger $l(\text{C-O})$ subgroup were studied as supports for metallic nanoparticles. For instance, Ni/LaAlO₃ is a catalyst for dry reforming of methane²⁵ at 700°C. It was shown that its catalytic performance is higher in terms of CO₂ and CH₄ conversion rates compared to Ni/La₂O₃ and Ni/Al₂O₃²⁵. All sites on considered lanthanum (III) oxide surfaces belong to the subgroup of smaller OCO-angles, whereas the sites on Al₂O₃ do not enter any of the two subgroups. KNbO₃ has been studied only with Pt nanoparticles and as a composite with g-C₃N₄ in photocatalytic reduction of CO₂ into CH₄^{21,22}. Pt-KNbO₃ is ~2.5 times more photoactive than Pt-NaNbO₃²¹, whereas the NaNbO₃ is known to be photoactive even without nanoparticles²³. This seems to suggest that $l(\text{C-O})$ is a good indicator of CO₂ activation for both unsupported and supported catalysts even at increased temperatures. Hence, the other materials with the sites from this subgroup are promising new candidates for this task. The most promising materials identified in this work are CsNbO₃, CsVO₃, RbVO₃, LaScO₃, GaInO₃, RbNbO₃, and NaSbO₃ as they have the sites from the larger $l(\text{C-O})$ subgroup satisfying the above mentioned criteria.

There is also a set of materials (ternaries $A^{2+}B^{4+}O_3$ ($A = \text{Ca, Sr, Ba, } B = \text{Zr, Ti, Ge, Sn, Si}$) with a perovskite structure) containing both the surfaces with sites from the smaller OCO subgroup and the surfaces with sites from the larger $l(\text{C-O})$ subgroup (Table 2). These two types of sites are located on different surfaces. Thus, based on the above results, a material for which a surface with sites from the larger $l(\text{C-O})$ subgroup has lower formation energy and is more abundant than the surface with sites from smaller OCO subgroup is expected to be a good catalyst. To explore this possibility, we analyze the surfaces of these materials in more detail. Their most stable surfaces are AO-terminated (001) facets containing sites from the smaller OCO subgroup. The formation energies of ABO₃-terminated (110) surfaces with larger $l(\text{C-O})$ sites are higher: for BaZrO₃, SrZrO₃, CaZrO₃, and SrTiO₃ the differences in formation energies are 0.049, 0.027, 0.013 and 0.037 eV/Å², respectively. The zirconates and SrTiO₃ were found to catalyze the water gas-shift reaction under increased temperatures, 700-1100 °C²⁷. At room temperature the photocatalytic activity of SrTiO₃ was found to be significantly decreased³². We attribute it to the strong carbonation of its most stable surface, which is consistent with the calculated high absolute value of CO₂ adsorption energy (-2.4 eV) for this surface. Thus, the activity of SrTiO₃ at 700 °C and higher temperatures is consistent with the estimates of the CO₂ chemical potential given above. The difference in formation energies of the most stable CaO-terminated (001) surface and the stoichiometric (110)

surface for CaTiO₃ is less pronounced compared to zirconates and other titanates (CaO-terminated (001) is more stable than the (110) surface by only 0.009 eV/Å²). Thus, the (110) facets, which contain sites from the long *l*(C-O) subgroup, may be present on catalyst particles at the reaction conditions. This can explain the observed activity of CaTiO₃ in CO₂ conversion not only at high but also at room temperature. We note that the activity of this material was also attributed to the presence of TiO₂ nanoparticles on the surface²⁸ at reaction conditions.

While we use properties of atomically *relaxed* surfaces as primary features, we have found that using bulk and gas-phase atomic features along with geometric features of *unrelaxed* bulk-terminated surfaces in SGD yields subgroups very similar in content to the larger *l*(C-O) subgroup, despite significant relaxation in some cases. One of best among such subgroups is defined by ($EN_{\min} \leq -2.88$ eV) AND ($d_2^{\text{unrelax}} \geq 2.18$ Å) AND ($r_{\max}^{\text{HOMO-1}} > 0.79$ Å) AND ($r_{\min}^{\text{HOMO-1}} \leq 1.03$ Å) AND ($\Delta_{\text{bulk}} < 4.32$ eV). For this set of materials the condition of larger distance to a second nearest cation (d_2) is very similar to the corresponding condition for the relaxed surfaces. The HOMO-1 radii ($r^{\text{HOMO-1}}$) reflect the sizes of cations in materials. The condition that the maximum radius among cations should not be too small and the minimum radius should not be too large indicates that the distance between the adsorption site and the cations at the surface matches an optimal range for bonding of the O atom in the adsorbed CO₂ molecule to a surface cation. More negative values of Mulliken electronegativity (EN) originate from more negative ionization potentials of B^{3+} and B^{5+} atoms, which were calculated as $E_{\text{atom}} - E_{\text{cation}}$ (Table 1). This, in turn, shows the electrophilicity of these cations, which is important in formation of chemical bonds with O-atoms of adsorbed CO₂. The unrelaxed surfaces subgroup contains 88% of samples from the larger *l*(C-O) subgroup based on primary features of relaxed surfaces. Among the rest, three sites have rather short values of *l*(C-O) – below 1.30 Å. In these cases the surface relaxation is significant. Except for LaAlO₃ all sites on materials from the Table 2 and those which we predict to be promising are in the subgroup obtained with unrelaxed features. Thus, even faster screening of materials and surfaces promising for CO₂ activation can be achieved, since calculations of surface relaxation and properties can be avoided. Promising surfaces predicted in this way can be further analyzed in terms of stability and relaxation effects for more accurate predictions.

Conclusions

We have developed a strategy for finding improved oxide-based catalysts for the conversion of chemically inert molecules such as CO₂. We identified an indicator of CO₂ activation — large C-O bond distance in the adsorbed molecule — applying data mining method subgroup discovery. This artificial-intelligence method showed the necessity for consideration of not only bulk and atomic properties, but also surface features for identification of the best semiconductor oxide

catalysts. The found subgroup selector, ($q_{\min} < 0.48 e$) AND ($W > 5.18 \text{ eV}$) AND ($d_2 > 2.14 \text{ \AA}$), which includes only the properties of clean relaxed surfaces, predicts whether a given candidate material belongs to the class of promising catalysts. Essentially the same subgroup is found when using only atomic and bulk features along with geometric features of unrelaxed bulk-terminated surfaces, which require substantially less computational effort. The checkup of experimental catalytic performance of materials with adsorption sites from the found subgroup showed that in all available studies they are active in different reactions of CO₂ conversion.

The present study shows that the previously proposed indicator, the decrease of the OCO angle¹⁵, is not sufficient to explain a high activity of the known oxide catalysts. In fact, small OCO angle is found to correlate with a strong adsorption, so that surfaces with corresponding adsorption sites are prone to carbonation. The other four considered potential indicators (charge of adsorbed CO₂, dipole moment, difference of charges on O-atoms and on C and O atoms of adsorbed CO₂) were also found to be unreliable. Using the above strategy, we propose several new oxide-based catalysts for CO₂ conversion, and the way for prediction of new materials initially from their bulk properties in a high-throughput manner. Finally, note that even if the present work has focused on oxides only, the overall strategy is general and can be applied to any other family of materials.

Acknowledgements

We thank Mario Boley for fruitful discussions on SGD and for providing the “Creedo” (for SGD) code. We also thank Yoshi Tateyama and Xinyi Lin for helping to generate the bulk oxide models and Helena Muñoz Galan and Oriol Lamiel Garcia for preliminary calculations. This project has received funding from the European Union’s Horizon 2020 research and innovation program (#676580: The NOMAD Laboratory — a European Center of Excellence and #740233: TEC1p).

Appendix: Other considered indicators of CO₂ activation

1. Dipole moment of the slab induced by adsorbed CO₂ molecule.

The dipole moment of the slab with adsorbed CO₂ molecule indicates both the bending of the molecule and the amount of charge transferred to the molecule upon adsorption (the dipole moment of the slab before adsorption is zero, since we use symmetrically terminated slabs), and thus it indicates the molecule activation. Since in our models the CO₂ adsorption was considered on one side of a surface slab, the dipole moment can be calculated as the difference of electrostatic potentials in vacuum at the two sides of the slab normalized per the surface area. The distribution of the calculated dipole moments in our data shows that certain number of samples has a positive dipole moment (Fig. A1, left), which is the result of surface relaxation upon CO₂ adsorption. We have performed SGD with the minimization of the dipole moment ($mm = \min$ in eq. 1 of the main

text), which corresponds to a larger amount of electron density transferred to the CO₂ molecule. The found subgroup ($q_{\min} \geq 0.44 e$) AND ($\alpha_{\max} \geq 76.45$) AND ($r^{\text{HOMO}-1}_{\min} \leq 1.085 \text{ \AA}$) AND ($r^{\text{LUMO}}_{\max} \leq 2.89 \text{ \AA}$) contains 41 samples with the distribution of values shown in Fig. A1, left. The overlap of this subgroup with the “larger $l(\text{C-O})$ ” subgroup is 2 samples, whereas it contains 24 common samples (59%) with the “smaller OCO” subgroup. In the Fig. A1 (right) the distribution of adsorption energies of samples from the considered subgroup is shown. Approximately half of samples have large absolute adsorption energies (above 2 eV), which is consistent with significant overlap with the “smaller OCO” subgroup. Regarding catalytic performance of samples with sites from obtained subgroup, the majority of them do not show increased activity since these materials are those which contain the sites from the “smaller OCO” subgroup (Table 1 in the main text).

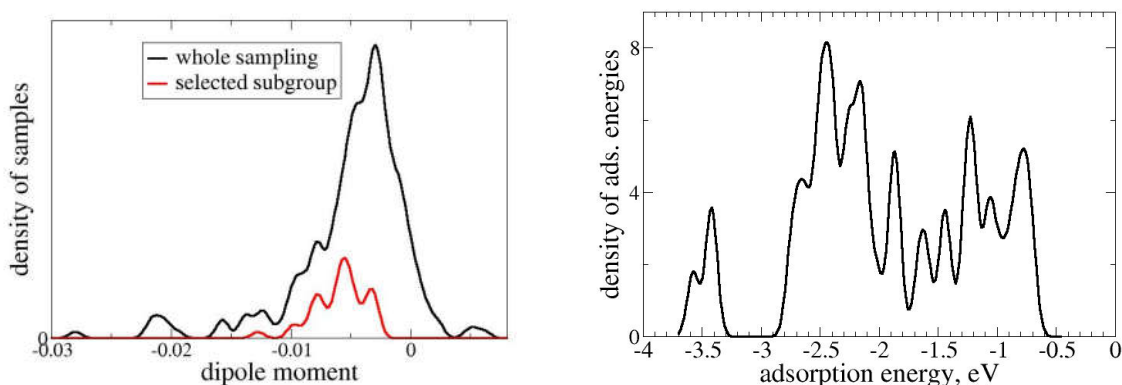


Figure A1. (left) The distribution of samples according to the calculated dipole moment in the whole data set (black) and in a subgroup with smaller dipole moments (red). (right) The distribution of adsorption energies in the subgroup of sites with larger dipole moments.

2. Hirshfeld charge of an adsorbed CO₂.

The physical reasoning behind this indicator is the same as in the case of the dipole moment. Although partitioning of electron density among atoms in a solid is not uniquely defined, different partitioning schemes and in particular Hirshfeld partitioning¹⁶ qualitatively capture changes in electron distribution. SGD was performed with the minimization of a negative median shift in eq. 1 of the main text. One of the found subgroups with high value of an objective function is defined by the condition ($q_{\text{O}} < -0.34 e$) AND ($w_{\max} \geq 1.14 \text{ eV}$) AND ($C_6^{\min} \geq 439.5 \text{ eV} \cdot \text{\AA}^6$) AND ($d_2 \geq 2.22 \text{ \AA}$). It contains 40 samples, and its overlap with “smaller OCO”/“larger $l(\text{C-O})$ ” is 25 (62,5%)/12 (30%) samples. Like for the previous indicator, the range of adsorption energies is quite broad (Figure A2). Again, there is a domain of samples with large absolute values of adsorption energies, which comes from the overlap with the “smaller OCO” subgroup. This is also the reason why catalytic activity in

CO₂ conversion for the majority of samples is low or absent at room and middle temperatures. Active materials are only those 30% which overlap with the “larger $l(\text{C-O})$ ” subgroup.

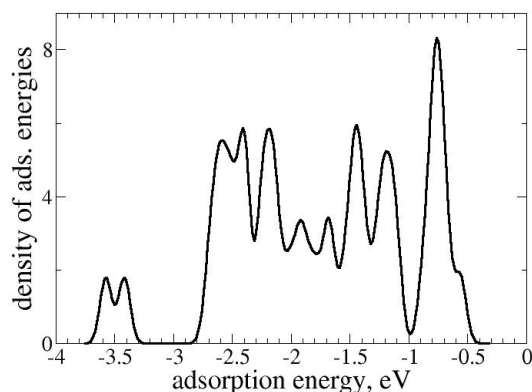


Figure A2. The distribution of adsorption energies in the subgroup of samples with larger absolute values of Hirshfeld charge of an adsorbed CO₂.

3. Difference in Hirshfeld charges of C and O atoms in an adsorbed CO₂

This property indicates the ionicity of a C-O bond. Larger ionicity is expected to correlate with the reactivity in reactions with electrophilic or nucleophilic agents. The calculated CO₂ gas-phase value of the charge difference is 0.44 e . It lies within the range of the data for adsorbed CO₂ 0.38-0.52 e (Fig. A3, left). The SGD search of subgroups with positive shift, implying larger ionicity, yields a subgroup of large size, 81 samples, ($V_{\text{BM}} > -5.99$ eV) AND ($L_{\text{min}} > -2.73$ eV). The distributions of the charge difference in the whole data set and in the subgroup are shown in Fig. A3, left. The overlap of the subgroup with “smaller OCO” is 48 samples (almost all samples in the latter), whereas the overlap with the “larger $l(\text{C-O})$ ” subgroup is 7 samples. As can be expected from this analysis, there are a lot of sites in this subgroup with large values of adsorption energies (Fig. A3, right). The overall distribution of adsorption energies is roughly the same as in the whole sampling. The catalytic performance of materials with sites from the obtained subgroup varies but stays low.

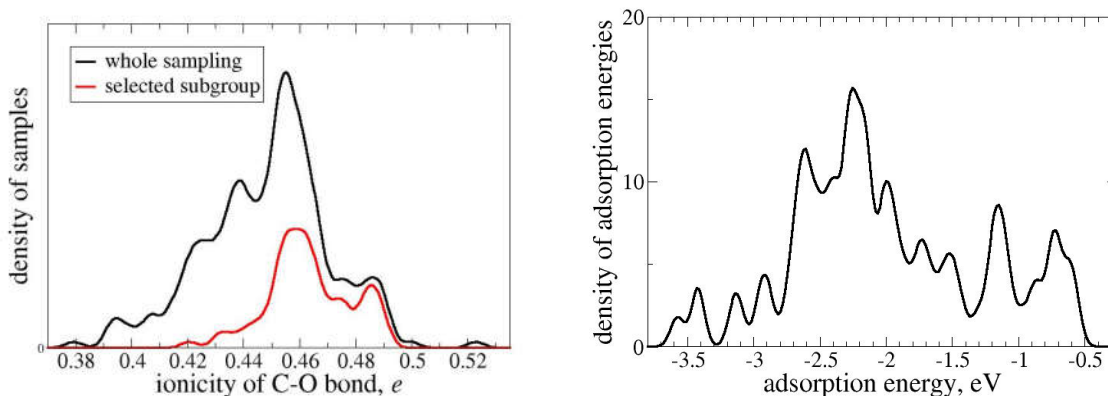


Fig. A3. (left) The distribution of samples according to the difference in Hirshfeld charges of C and O atoms (ionicity of C-O bond) in an adsorbed CO₂ for the whole data set (black) and for a subgroup with larger ionicity (red). (right) The distribution of adsorption energies in the subgroup with larger ionicity.

Among subgroups with a highest quality function there is also a small-sized subgroup ($M > -4.65$ eV) AND ($IP_{\min} \geq -7.29$ eV) AND ($E_{\text{form}} \geq 0.04$ eV/Å²) with 14 samples only. All sites in this subgroup belong also to the “smaller OCO” subgroup and have very high values of adsorption energies.

4. Difference of Hirshfeld charges on O-atoms of an adsorbed CO₂

As it was found in the case of the “larger $l(\text{C-O})$ ” subgroup, the elongated C-O bonds are observed when the CO₂ molecule is adsorbed in an asymmetric position, so that one oxygen atom is bonded with a surface cation and the other one is protruding. In these cases, the two O-atoms have nonequivalent chemical surroundings. Correspondingly, the difference of Hirshfeld charges on CO₂ oxygens is expected to indicate this asymmetry. The SGD with the absolute charge difference as target property was performed with positive median shift in the quality function (1) in the main text.

A found subgroup ($q_{\max} > 0.58$ eV) AND ($IP_{\max} > -5.70$) AND ($EA_{\min} \geq -0.72$ eV) AND ($d_1 < 1.99$) contains about 12% of all samples. 14 samples are common with the “larger $l(\text{C-O})$ ” subgroup, mainly ANbO₃ ($A = \text{Na, K, Rb, Cs}$), and 2 samples are common with the “smaller OCO” subgroup. The niobates were found to be catalytically (photo)active in CO₂ conversion as described in the main text. Also there is another photoactive material in this subgroup, LiNbO₃³⁴, which is not in the “larger $l(\text{C-O})$ ” subgroup though. However, other catalytically active materials from the “larger $l(\text{C-O})$ ” subgroup do not enter this subgroup.

The distribution of adsorption energies in the found subgroup is shown in Fig. A4. The majority of sites have adsorption energies with middle values: (-0.5, -1.5) eV. The sites common

with the “large $|(C-O)|$ ” subgroup belong exactly to this range. However, there is a subset of samples with the energies around -2 eV (up to -2.3 eV). They are sites with largest absolute CO₂ adsorption energy on InAlO₃-orthorhombic (121), InScO₃ (100) and (110) surfaces. The first two surfaces are by far not the most stable for a given material. The third one has the formation energy very close to the most stable facet on InScO₃. In the literature there are no data regarding catalytic activity of InScO₃ and InAlO₃ in CO₂ conversion.

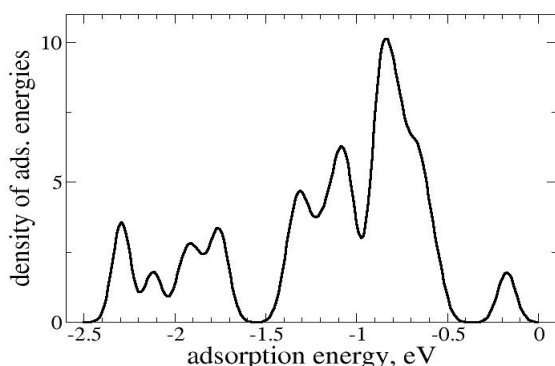


Figure A4. The distribution of adsorption energies in the subgroup with larger absolute difference of O-charges in an adsorbed CO₂.

References

1. H. Arakawa et al. Catalysis research of relevance to carbon management: progress, challenges, and opportunities. *Chem. Rev.* **2001**, *101*, 953–996.
2. G.A. Olah. Beyond oil and gas: the methanol economy. *Angew. Chem. Int. Ed.* **2005**, *44*, 2636–2639. G.A. Olah, A. Goepfert, G.K. Surya Prakash. Chemical recycling of carbon dioxide to methanol and dimethyl ether: from greenhouse gas to renewable, environmentally carbon neutral fuels and synthetic hydrocarbons. *J. Org. Chem.* **2009**, *74*, 487–498.
3. G.A. Somorjai. Introduction to Surface Chemistry and Catalysis. **2010**.
4. J.K. Nørskov, F. Studt, F. Abild-Pedersen, T. Bligaard. Fundamental Concepts in Heterogeneous Catalysis. **2014**.
5. J.A. Martens, A. Bogaerts, N. De Kimpe, P.A. Jacobs, G.B. Marin, K. Rabaey, M. Saeys, S. Verhelst. The Chemical Route to a Carbon Dioxide Neutral World. *ChemSusChem.* **2017**, *10*, 1039-1055.
6. J. Klankermayer, S. Wesselbaum, K. Beydoun, W. Leitner. Selective catalytic synthesis using the combination of carbon dioxide and hydrogen: catalytic chess at the interface of energy and chemistry. *Angew. Chem. Int. Ed.* **2016**, *55*, 7296-7343.

7. J. Artz, T.E. Müller, K. Thenert, J. Kleinekorte, R. Meys, A. Sternberg, A. Bardow, W. Leitner. Sustainable conversion of carbon dioxide: an integrated review of catalysis and life cycle assessment. *Chem. Rev.* **2018**, *118*, 434-504.
8. W. Li, H. Wang, X. Jiang, J. Zhu, Z. Liu, X. Guo, C. Song. A short review of recent advances in CO₂ hydrogenation to hydrocarbons over heterogeneous catalysts. *RSC Adv.* **2018**, *8*, 7651-7669.
9. N.A. Richter, S. Siculo, S.V. Levchenko, J. Sauer, M. Scheffler. Concentration of vacancies at metal-oxide surfaces: case study of MgO(100). *Phys. Rev. Lett.*, **2013**, *111*, 045502.
10. S. Arndt, G. Laugel, S. Levchenko R. Horn, M. Baerns, M. Scheffler, R. Schlögl, and R. Schomäcker. A critical assessment of Li/MgO-based catalysts for the oxidative coupling of methane. *Cat. Rev. Sci. Eng.* **2011**, *53*, 424-514.
11. Z. Yan, S. Chinta, A. A. Mohamed, J. P. Fackler, D. W. Goodman. The role of f-centers in catalysis by Au supported on MgO. *J. Am. Chem. Soc.* **2005**, *127*, 1604-1605.
12. A.K. Singh, J.H. Montoya, J.M. Gregoire, K.A. Persson. Robust and synthesizable photocatalysts for CO₂ reduction: a data-driven materials discovery. *Nat. Comm.* **2019**, *10*, 443.
13. P. Schlexer Lamoureux, K.T. Winther, J.A. Garrido Torres, V. Streibel, M. Zhao, M. Bajdich, F. Abild-Pedersen, T. Bligaard. Machine learning for computational heterogeneous catalysis. *ChemCatChem* **2019**, *11*, 3581-3601.
14. J.P. Perdew, A. Ruzsinszky, G.I. Csonka, O.A. Vydrov, G.E. Scuseria, L.A. Constantin, X. Zhou, K. Burke. Restoring the density-gradient expansion for exchange in solids and surfaces. *Phys. Rev. Lett.*, **2008**, *100*, 136406.
15. H.-J. Freund, M. W. Roberts. Surface chemistry of carbon dioxide. *Surf. Sci. Rep.* **1996**, *25*, 225-273.
16. F.L. Hirshfeld. Bonded-atom fragments for describing molecular charge densities. *Theor. Chim. Acta*, **1977**, *44*, 129-138.
17. M. Boley, B. Goldsmith, L.M. Ghiringhelli, J. Vreeken. Identifying consistent statements about numerical data with dispersion-corrected subgroup discovery. *Data Min. Knowl. Disc.* **2017**, *31*, 1391-1418.
18. B. Goldsmith, M. Boley, J. Vreeken, M. Scheffler, L.M. Ghiringhelli. Uncovering structure-property relationships of materials by subgroup discovery. *New J. Phys.* **2017**, *19*, 013031.
19. M. Khraisheh, A. Khazndar, M.A. Al-Ghouti. Visible light-driven metal-oxide photocatalytic CO₂ conversion. *Int. J. Energy Res.* **2015**, *39*, 1142-1152.

20. T. Ishihara, K.T. Wu, S. Wang. High temperature CO₂ electrolysis on La(Sr)Fe(Mn)O₃ oxide cathode by using LaGaO₃ based electrolyte. *ECS Transactions*, **2015**, *66*, 197-205.
21. H. Shi, Z. Zou. Photophysical and photocatalytic properties of ANbO₃ (A=Na, K) photocatalysts. *J. Phys. and Chem. Sol.* **2012**, *73*, 788-792.
22. H. Shi, C. Zhang, C. Zhou, G. Chen. Conversion of CO₂ into renewable fuel over Pt-g-C₃N₄/KNbO₃ composite photocatalyst. *RSC Adv.*, **2015**, *5*, 93615-93622.
23. F. Fresno, P. Jana, P. Reñones, J.M. Coronado, D.P. Serrano, V.A. de la Peña O'Shea. CO₂ reduction over NaNbO₃ and NaTaO₃ perovskite photocatalysts. *Photochem. Photobiol. Sci.*, **2017**, *16*, 17-23.
24. G.V. Nizova, G. Süß-Fink, S. Stanislas, G.B. Shul'pin. Carboxylation of methane with CO or CO₂ in aqueous solution catalysed by vanadium complexes. *Chem. Comm.* **1998**, *17*, 1885-1886.
25. Y. Kathiraser, W. Thitsartarn, K. Sutthiumporn, S. Kawi. Inverse NiAl₂O₄ on LaAlO₃-Al₂O₃: unique catalytic structure for stable CO₂ reforming of methane. *J. Phys. Chem. C*, **2013**, *117*, 8120-8130.
26. M.T. Dunstan, A. Jain, W. Liu, S. Ping Ong, T. Liu, J. Lee, K.A. Persson, S.A. Scott, J.S. Dennis, C.P. Grey. Large scale computational screening and experimental discovery of novel materials for high temperature CO₂ capture. *Energy Environ. Sci.*, **2016**, *9*, 1346-1360.
27. Y. Saito. *Patent No.:* US 8,540,898 B2; Sep. 24, **2013**.
28. B. Sub Kwak, M. Kang. Photocatalytic reduction of CO₂ with H₂O using perovskite Ca_xTi_yO₃. *Appl. Surf. Sci.*, **2015**, *337*, 138-144.
29. H. Muroyama, Y. Tsuda, T. Asakoshi, H. Masitah, T. Okanishi, T. Matsui, K. Eguchi. Carbon dioxide methanation over Ni catalysts supported on various metal oxides. *J. Catal.* **2016**, *343*, 178-184.
30. Z. Zhang, X.E. Verykios, S.M. MacDonald, S. Affrossman. Comparative study of carbon dioxide reforming of methane to synthesis gas over Ni/La₂O₃ and conventional nickel-based catalysts. *J. Phys. Chem.* **1996**, *100*, 744-754.
31. J.H. Lee, J.Y. Do, N.-K. Park, M.W. Seo, H.-J. Ryu, J.-P. Hong, Y.S. Kim, S.K. Kim, M. Kang. Cost-effective and dynamic carbon dioxide conversion into methane using a CaTiO₃@Ni-Pt catalyst in a photo-thermal hybrid system. *J. Photochem. Photobiol. A: Chem.* **2018**, *364*, 219-232.
32. S. Zeng, P. Kar, U.K. Thakur, K. Shankar. A review on photocatalytic CO₂ reduction using perovskite oxide nanomaterials. *Nanotechnology*. **2018**, *29*, 052001.

33. D. Stull and H. Prophet, JANAF Thermochemical Tables, 2nd edn. U.S. National Bureau of Standards, Washington, D.C., **1971**.
34. M. Stock, S. Dunn. LiNbO₃ – a new material for artificial photosynthesis. *IEEE Trans. Ultrason. Ferroelectr. Freq. Control.* **2011**, 58, 1988-1993.

Supplementary information

Ab initio methodology

All *ab initio* calculations were performed with the all-electron full-potential electronic structure FHI-aims code package [1] using density-functional theory (DFT) and numerical atom-centered basis functions. The standard 'tight' settings (grids and basis functions) were employed [1], which deliver the adsorption energies with basis-set superposition errors below 0.07 eV per adsorbed molecule. The exchange-correlation (XC) functional approximation was chosen based on a comparison to available experimental and high-level theoretical data on CO₂ adsorption energy (see below). PBE [2] and PBEsol [3] functionals with and without Tkatchenko-Scheffler (TS) pairwise dispersion-correction method [8] were tested. LDA [4] and RPBE [5] have been previously shown to give large errors for adsorption of CO₂ [6,7]. All systems were treated as spin non-polarized. The bulk lattice vectors were calculated with the same exchange-correlation functional as the surface and the adsorbed molecule properties. The *k*-points for the bulk calculations were converged with respect to lattice vectors. The slabs were symmetric and all atoms therein were allowed to relax. We did not constrain any side of a slab in order to have the same surface geometry on both sides, which is important for calculation of surface primary features. The slab thickness was also tested and it was set to about 11 Å or larger in most cases, based on the convergence of the surface energy (within 5 meV/Å²) and the work function (within 10 meV) with respect to the thickness. For the surface supercells the *k*-grids were scaled from corresponding bulk grids. The lattice constants were obtained from the relaxed bulk unit cells. The initial geometries of adsorbed CO₂ before full atomic relaxation were obtained by placing the CO₂ molecule at different possible adsorption sites (metal and O sites, top, bridge, and hollow sites) and in different orientations (C down, O down) on one side of the slab. The size of the surface supercells was set based on test calculations, so that the interaction between the periodic images of the adsorbed CO₂ was below 0.1 eV. The resulting distance between the images of the C atom was about 8 Å. The adsorption of CO₂ has been considered only on one side of the slab, and a dipole correction [9] was included to prevent spurious electrostatic interactions. The lattice vector along the direction parallel to the vacuum gap was 200 Å. All atoms in the systems have been allowed to relax until the maximum remaining force fell below 10⁻² eV/Å.

There are a few experimental data available for CO₂ adsorption at clean monocrystalline surfaces without impurities: at CaO (001) [10] and at ZnO (10-10) [11,12]. We compared the calculated adsorption energies (E_{ads}) to the microcalorimetry and temperature programmed desorption (TPD) data. The adsorption energies were calculated as the difference between total energies of the slab with the adsorbed molecule, clean surface slab, and a free gas-phase CO₂

molecule. The calculations of the surfaces were performed with symmetric 5-atomic layer slabs for CaO (001) and 4 double-layer slab for ZnO (10-10). $8 \times 8 \times 8$ and $10 \times 10 \times 6$ k-point grids were used for cubic CaO and hexagonal ZnO bulk unit cells, respectively. Surface unit cells were (2x2) for CaO (001), for ZnO (10-10) we considered two cells – (1x1) and (1x2).

The results for CaO (001) and ZnO (10-10) are shown in Table S1. In the case of CaO the PBE adsorption energy is the closest to the experimentally observed value both from TPD and microcalorimetry, whereas PBEsol and PBEsol+TS values are closer to the one obtained with CCSD(T) using an embedded cluster model [10]. The inconsistency of the high-level theoretical and the experimental results was explained [10] by the formation of agglomerates of adsorbed CO₂ molecules even in ultrahigh-vacuum. Relative to CCSD(T), PBEsol+TS performs better.

Table S1. The experimental and theoretical energies of adsorption (in eV) of CO₂ at CaO (001) and ZnO (10-10) surfaces.

method	CaO (001)	ZnO (10-10)		MgO (001)
		(1x1) structure	(1x2) structure	
PBE	-1.32	-0.45	-0.67	-0.34
PBE+TS	-1.47	-0.79	-0.96	-0.53
PBEsol	-1.60	-0.84	-1.04	-0.63
PBEsol+TS	-1.75	-1.00	-1.19	-0.79
TPD	-1.24 – -1.45 [10]	-0.55 [11]	-0.90 [11,12]	-0.41 [14]
microcalorimetry	~ -1.30 [10]	-0.72 [12]	-1.12 [12]	-
high-level calculations	-1.91 ± 0.10 ^a [10]	-	-	-0.64 ^b [15]

^aCCSD(T); ^bHSE(0.3)+vdW

In the case of ZnO (10-10) the experimental data have been obtained for two adsorption coverages: 100% [(1x1) structure] and 50% [(1x2) structure]. In contrast to CaO, TPD and microcalorimetry values differ by about 0.2 eV (Table S1). Taking into account that the calculated thermo-desorption energies depend on the chosen kinetic model as well as on the pre-exponential factor, we consider the microcalorimetry results as more accurate. The PBEsol adsorption energies match both measured values with the best accuracy (~0.1 eV). PBEsol+TS slightly overestimates the adsorption energies. It is not unexpected, since PBEsol functional behaves similarly to LDA for interatomic interactions at the middle-range distances, so that inclusion of additional vdW-correction leads to overestimation of binding energies. In addition, the TS scheme based on non-iterative Hirshfeld partitioning of the electron density was found to fail in predicting adsorption energies for some ionic systems, due to inaccurate description of polarizabilities [13].

We also compare the GGA CO₂ adsorption energies for MgO (001) surface with hybrid HSE(0.3)+vdW functional results [15], where HSE(0.3)+vdW is the HSE functional with 30% fraction of exact exchange plus the many-body dispersion correction [20]. This functional was shown to yield CO₂ adsorption energies very close to CCSD(T) for embedded clusters [15], and the adsorption energy was found to be -0.64 eV. The closest value was obtained with the PBEsol functional (-0.63 eV). Thus, PBEsol compares favorably to both experiment and higher-level calculations. In addition to the above mentioned systems, two more systems were tested: CO₂ adsorption on BaO-terminated BaTiO₃ (001) and on CaZrO₃ (101) surfaces. In general, we find that *relative differences* in adsorption energy between different XC approximations are weakly dependent on the material and surface termination (Figure S1, left).

In addition to adsorption energies, another important parameter of CO₂ adsorption is the OCO angle, which is 180° in the neutral gas-phase molecule and close to 120° (as in a gas-phase CO₃²⁻ ion) in adsorbed systems. As there are no precise experimental data like in the case of adsorption energies, here we rely on a weak sensitivity of the OCO angle to XC functional approximations. PBE, PBE+TS, and PBEsol provide very close OCO-angles for all tested systems (Figure S1, right). The largest difference was observed in MgO (001) case where PBE+TS value is larger than PBE and PBEsol by 1.0°. In all other cases such deviation was 0.4 degree on average.

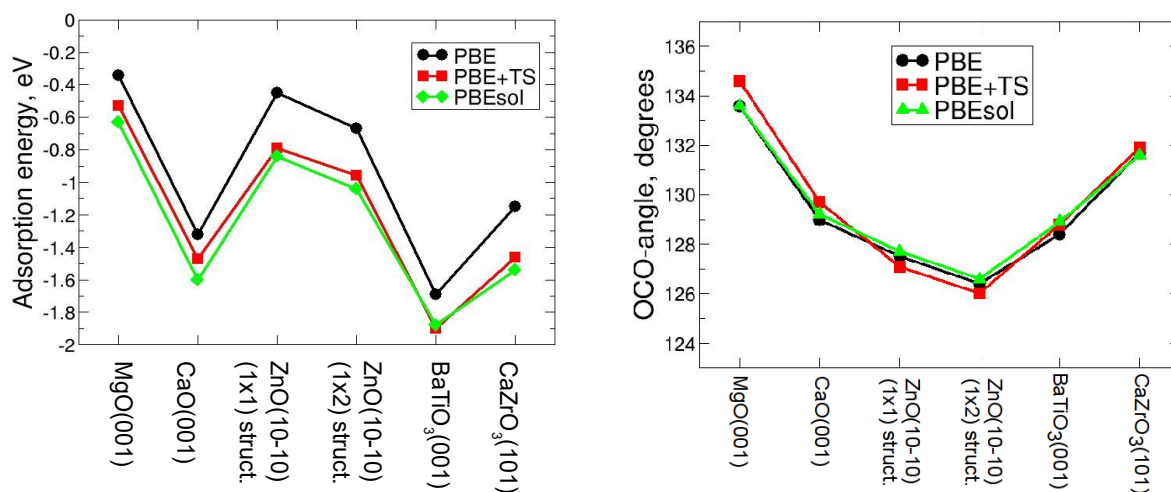


Figure S1. The adsorption energies (left) and OCO-angles (right) of adsorbed CO₂ for different surfaces and XC functionals.

Summarizing the test results, and taking into account that PBEsol provides a very good agreement between calculated and experimental bulk lattice constants for ionic solids [3], we conclude that PBEsol is the best choice for our study.

Studied materials and surface terminations

In the current study we have focused on semiconductor oxide materials (binary and ternary). In general three groups of oxides have been considered: $A^{2+}B^{4+}O_3$, $A^{1+}B^{5+}O_3$, $A^{3+}B^{3+}O_3$ and all the binary oxides AO , BO_2 , A_2O_3 , A_2O , B_2O_3 . For each oxide material we have considered a set of low-index surfaces with maximal Miller index up to 2. We mainly considered non-polar surfaces. For several included polar surfaces, reconstructions that compensate surface charge assuming formal charges of the ions were considered. All surfaces were insulating (with a non-vanishing gap between the highest occupied and lowest unoccupied states). In the cases when oxides have polymorphs (TiO_2 , $MgGeO_3$ etc.) they were also included. The full list of materials and surface terminations is shown in Table S2. In general, 71 materials have been calculated with 141 surfaces including different terminations. Considering all non-equivalent adsorption sites on these surfaces, the total number of calculated unique CO_2 adsorption geometries is 270. All data, including initial and final geometries, and the computed properties, are available in the NOMAD database [16].

Table S2. Oxide materials, surface terminations, and the number of unique adsorption sites per termination.

material	surfaces	number of unique sites per surface
$MgSiO_3$	(001) MgO-term.	1
$MgTiO_3$	(001) (012)	1 2
$MgGeO_3$ hexagon.	(001) (012)	1 2
$MgGeO_3$ tetragon.	(001) MgO-term. (001) GeO_2 -term.	1 1
$MgSnO_3$	(100)	2
$CaSiO_3$	(001) CaO-term. (001) SiO_2 -term. (110) CaO-term. (110) SiO_2 -term.	1 1 1 1
$CaTiO_3$	(010) CaO-term. (101) CaO-term. (100) TiO_2 -term.	1 1 1
$CaGeO_3$	(001) CaO-term. (001) GeO_2 -term. (110) CaO-term. (110) GeO_2 -term.	1 2 1 2
$CaZrO_3$	(010) CaO-term. (101) CaO-term. (101) ZrO_2 -term.	1 2 1
$CaSnO_3$	(001) SnO_2 -term. (110) CaO-term. (110) SnO_2 -term.	1 2 1
$SrSiO_3$	(001) SrO-term.	1
$SrTiO_3$	(001) SrO-term.	1

	(001) TiO ₂ -term.	1
SrGeO ₃	(100) SrO-term.	1
	(100) TiO ₂ -term.	1
SrZrO ₃	(001) ZrO ₂ -term.	1
	(110) SrO-term.	2
SrSnO ₃	(001) SrO-term.	1
	(001) SnO ₂ -term.	1
	(110) SrO-term.	1
	(110) SnO ₂ -term.	1
BaSiO ₃	(100)	2
	(101)	1
BaTiO ₃	(001) BaO-term.	1
	(001) TiO ₂ -term.	1
BaGeO ₃	(001) BaO-term.	1
BaZrO ₃	(001) ZrO ₂ -term.	1
	(110) BaO-term.	1
BaSnO ₃	(001) BaO-term.	1
	(001) SnO ₂ -term.	1
MgO	(001)	1
	(110)	1
	(111) oct. O-term.	1
CaO	(001)	1
	(110)	1
	(111) oct. O-term.	1
SrO	(001)	1
	(110)	1
	(111) oct. O-term.	1
BaO	(001)	1
	(110)	1
	(111) oct. O-term.	1
SiO ₂	(001)	2
TiO ₂ anatase	(101)	2
	(001)	1
TiO ₂ rutile	(100)	1
	(110)	2
GeO ₂	(100)	1
	(110)	2
ZrO ₂	(001)	2
	(011)	4
	(111)	3
SnO ₂	(100)	1
	(110)	2
ZnO	(10-10)	1
LiNbO ₃	(100)	1
NaNbO ₃ tetragon.	(010)	2
	(110)	1
NaNbO ₃ P bcm	(100)	1
KNbO ₃ tetragon.	(010)	1
	(110)	2
RbNbO ₃ P1	(111)	2

CsNbO ₃	(010)	2
	(100)	1
LiVO ₃ orthogon.	(110)	2
LiVO ₃ P bcm	(100)	1
NaVO ₃	(010)	1
	(110)	1
KVO ₃ orthogon.	(010)	1
RbVO ₃ tetragon.	(010)	1
	(110)	1
RbVO ₃ P bcm	(100)	1
CsVO ₃ tetragon.	(010)	1
	(110)	1
LiSbO ₃ tetragon.	(010)	1
LiSbO ₃ P bcm	(100)	1
NaSbO ₃ tetragon.	(010)	1
NaSbO ₃ P bcm	(100)	2
KSbO ₃ tetragon.	(110)	2
Na ₂ O	(011)	1
	(111)	1
GaAlO ₃	(100)	2
InAlO ₃ hexagon.	(110)	2
InAlO ₃ orthorh.	(010)	3
	(110)	4
	(121)	3
GaInO ₃	(100)	2
	(110)	5
	(120)	6
ScAlO ₃	(010)	1
	(100)	2
	(110)	2
	(121)	6
ScGaO ₃	(010)	3
	(110)	5
ScInO ₃	(100)	5
	(110) In ₂ O ₃ -term.	5
	(110) ScInO ₃ -term.	5
	(121)	6
YScO ₃	(100)	1
LaScO ₃	(100)	1
YInO ₃	(100)	2
	(110)	2
YAlO ₃	(011)	2
	(100)	1
LaYO ₃	(001)	2
YGaO ₃	(100)	2
	(110)	2
LaAlO ₃	(110)	2
LaGaO ₃	(100)	1
	(110)	1

LaInO ₃	(100)	1
Al ₂ O ₃	(001)	1
	(012)	1
Ga ₂ O ₃	(110)	3
	(212)	7
Sc ₂ O ₃	(001)	3
	(110)	5
	(111)	5
In ₂ O ₃	(001)	1
	(110)	5
	(111)	4
La ₂ O ₃	(100)	2
	(110)	2
	(120)	3
	(201)	2

Table S3. The options applied in the program Creedo in subgroup discovery (for more details see the references 17 and 18 in the main text).

Group mappers	Consecutive_change_attributes, distribution_mode, distribution_shape, distribution_median
Attribute mappers	Smart_discrete_ordinal, positive_and_negative, clustering_14_cutoffs
Category	Exceptional subgroup discovery
Algorithm	Randomized Exceptional subgroup discovery
Model class	Empirical distribution
Seed distribution	$P(x)=\text{freq}(x)^a$
a	1
Post processing	LinearRandomPruner

Subgroup discovery with the OCO-angle as a target property

Among 270 considered adsorption sites, in 23 cases the physisorption is energetically more stable than the chemisorption. In the physisorbed case, the CO₂ molecule is not activated. Since there is no charge transfer from the surface, its OCO-angle remains to be around 180° and the C-O bond distance 1.17 Å as in the gas phase. The overall distribution of OCO-angles is shown in Figure S2 (black).

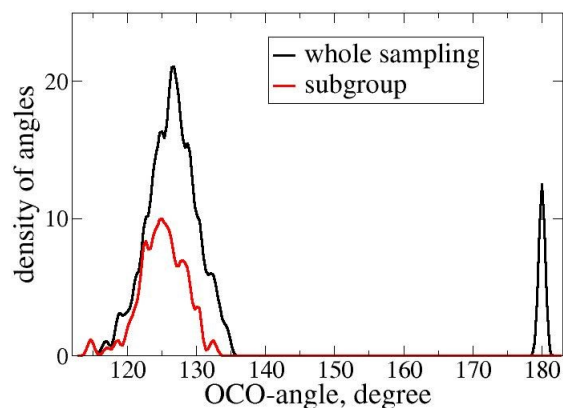


Figure S2. The distribution of OCO-angles for the whole sampling (black) and for the subgroup found with SGD based on all data.

The subgroup discovery performed by minimizing OCO-angle using the quality function (1) in the main text identifies a subgroup ($q_O < -0.35$ e) AND ($\varphi_{1.4} > 0.35$ eV) AND ($EA_{\min} \leq 0.005$ eV) AND ($d_1 \geq 1.83$ eV) which covers 42% of samples. The distribution of samples in the subgroup is rather broad (Figure S2, red) if we consider only the “chemisorbed” domain. The subgroup contains sites with small, middle and large OCO-angles. Such a broad distribution is explained by the fact that the value of an absolute median deviation for the whole sampling ($\text{amd}(Y)$) is quite large (7.15°) when compared to the whole range of OCO angles (115° - 180°). Correspondingly the narrowness term in the quality function, $(1 - \text{amd}(Z)/\text{amd}(Y))$, has already a relatively large value for the whole “chemisorbed” domain. Therefore, since we are interested in the sites delivering small OCO-angles from the “chemisorbed” domain, we perform data analysis including data only from this domain, as described in the main text. The obtained SGD selectors will automatically select materials that fall within the “chemisorbed” domain, since only these materials provide smaller OCO angles and longer C-O bonds.

Table S4. The full list of used primary features calculated with PBEsol.

symbol	meaning
$IP_{\min/\max}$, IP_O	ionization potential, minimal and maximal in the pair of atoms A and B , and for O; calculated as $E_{\text{atom}} - E_{\text{cation}}$
$EA_{\min/\max}$, EA_O	electron affinity, minimal and maximal in the pair of atoms A and B , and for O; calculated as $E_{\text{anion}} - E_{\text{atom}}$
$EN_{\min/\max}$, EN_O	Mulliken electronegativity, minimal and maximal in the pair of atoms A and B , and for O
r_{HOMO} , r_{+1} , r_{-1}	maximum value of radial wave functions of the non-spin polarized spherically symmetric atom for HOMO, LUMO and HOMO-1

Δ	band gap of the whole surface slab
E_{form}	surface formation energy
VBM	valence-band maximum with respect to vacuum level
W	work function ($W = -VBM$)
q_{O}	Hirshfeld charge of O-atom
$q_{\text{min}}, q_{\text{max}}$	minimal and maximal Hirshfeld charges of cations in the pair A and B , calculated as an average for all surface cations of a given type
$\varphi_{1.4}, \varphi_{2.6}, \varphi_{1.4} - \varphi_{2.6}$	electrostatic potentials above O-atom at 1.4 and 2.6 Å and their difference. 1.4 Å corresponds to the average length of the bond between C and surface O, 2.6 Å is the minimal distance from surface O to C-atom of physisorbed carbon-dioxide molecule as observed from our calculations
$\alpha_{\text{O}}, C_6^{\text{O}}$	polarizability and C_6 -coefficient for O-atom obtained from many-body dispersion scheme [20]
$\alpha_{\text{min}}, \alpha_{\text{max}}, C_6^{\text{min}}, C_6^{\text{max}}$	polarizability and C_6 -coefficient for cations, minimal and maximal in the pair A and B , calculated as an average for all surface cations of a given type
Q_5, Q_6	local-order parameter with $l = 5$ or 6
d_1, d_2, d_3	distances from surface O-atom to the first-, second-, and third-nearest cations
BV	bond-valence value of O-atom
PC	weighted O $2p$ -band center
$c_{\text{min}}, c_{\text{max}}$	first moment for PDOS of cation within valence-band, minimal and maximal in the pair A and B , calculated as an average for all surface cations of a given type
wid	square-root from the second moment of O $2p$ -band
$wid_{\text{min}}, wid_{\text{max}}$	square-root of the second moment for PDOS of cations within valence-band, minimal and maximal in the pair A and B , calculated as an average for all surface cations of a given type
$skew$	skewness of O $2p$ -band PDOS
$kurt$	kurtosis of O $2p$ -band PDOS
CBm	conduction band minimum
$L_{\text{min}}, L_{\text{max}}$	energy of lowest unoccupied state of cation, minimal and maximal in the pair A and B , calculated as an average for all surface cations of a given type
M	energy at which the O $2p$ -band PDOS is maximal
U	eigenstate with least negative value in O $2p$ -band
$\varepsilon^{\text{LUMO}}(\text{CO}_2)$	energy of the gas-phase CO_2 LUMO (was never chosen during SISSO)

Alternative subgroups found by SGD.

The search of subgroups is done in a stochastic way with adapted Monte-Carlo algorithm for these purposes. The uniqueness of identified subgroups is characterized by quality function (eq. 1 in the main text). Thus, besides described subgroups of sites with larger $l(\text{C-O})$ or smaller OCO -angles the algorithm generates many other subgroups and sorts them according to quality function. In the

Tables S5 and S6 the other found top subgroups are presented. Comparing to larger $l(\text{C-O})$ subgroup ($q_{\min} < 0.48 e$) AND ($W > 5.18 \text{ eV}$) AND ($d_2 > 2.14 \text{ \AA}$), other subgroups have similar definitions and considerable overlap, although their size shows that some of them are too specific (Table S5). The choice of mentioned subgroup was done based on its larger size and high value of quality function. Similarly, the subgroup of smaller OCO-angles ($M > -6.0 \text{ eV}$) AND ($d_1 \geq 1.80 \text{ \AA}$) AND ($d_2 > 2.14 \text{ \AA}$) has large overlap with other top subgroups, similar definitions and close value of quality function (Table S6). We selected it as a statistically averaged subgroup from the top of list.

Table S5. Alternative subgroups identified by SGD maximizing $l(\text{C-O})$. The value of quality function in the large $l(\text{C-O})$ subgroup is 0.0153.

definition	size	overlap with long $l(\text{C-O})$, %	Quality function
$(q_{\min} < 0.53 e)$ AND $(IP_{\min} < -6.39 \text{ eV})$ AND $(EA_{\max} < 0.04 \text{ eV})$ AND $(kurt > 3.13)$	18	83	0.0169
$(W < 6.78 \text{ eV})$ AND $(IP_{\min} < -6.47 \text{ eV})$ AND $(EA_{\max} < 0.00 \text{ eV})$ AND $(EN_{\max} > -3.41 \text{ eV})$ AND $(kurt > 2.51)$	17	88	0.0150
$(q_{\min} < 0.48 e)$ AND $(q_{\max} > 0.42 e)$ AND $(d_1 < 1.85 \text{ \AA})$ AND $(d_2 > 2.14 \text{ \AA})$	22	95	0.0146
$(q_{\min} < 0.56 e)$ AND $(CBm < -2.28 \text{ eV})$ AND $(EN_{\max} < -3.17 \text{ eV})$ AND $(C_6^{\max} > 451)$ AND $(d_1 < 1.85 \text{ \AA})$ AND $(d_2 > 2.0 \text{ \AA})$	24	79	0.0145
$(q_{\min} < 0.48 e)$ AND $(q_{\max} > 0.47 e)$ AND $(\varphi_{2.6} > -0.12 \text{ eV})$ AND $(d_2 > 2.10 \text{ \AA})$ AND $(r_{-1}^{\max} > 1.14 \text{ \AA})$	27	85	0.0142

Table S6. Alternative subgroups identified by SGD minimizing OCO angle. The value of quality function in the small OCO subgroup is 0.0146

definition	size	overlap with long $l(\text{C-O})$, %	Quality function
$(wid < 1.59 \text{ eV})$ AND $(W < 5.87 \text{ eV})$ AND $(d_1 > 1.82 \text{ \AA})$ AND $(d_2 > 2.14 \text{ \AA})$ AND $(skew < -0.38)$	42	95	0.0157
$(W < 5.87 \text{ eV})$ AND $(CBm > -3.72 \text{ eV})$ AND $(\varphi_{1.4} > 1.50 \text{ eV})$ AND $(d_1 > 1.82 \text{ \AA})$ AND $(d_2 > 2.07 \text{ \AA})$	46	91	0.0149
$(M > -6.04 \text{ eV})$ AND $(wid < 1.69 \text{ eV})$ AND $(d_1 \geq 1.85 \text{ \AA})$ AND $(d_2 > 2.14 \text{ \AA})$	43	100	0.0148
$(W < 5.75 \text{ eV})$ AND $(\varphi_{1.4} > 1.50 \text{ eV})$ AND $(d_1 > 1.79 \text{ \AA})$ AND $(d_2 > 2.07 \text{ \AA})$	46	91	0.0145

$(W < 5.75 \text{ eV}) \text{ AND } (\varphi_{2.6} > 0.09 \text{ eV}) \text{ AND } (d_1 > 1.85 \text{ \AA})$ $\text{AND } (d_2 > 2.14 \text{ \AA}) \text{ AND } (\textit{skew} < -0.38)$	38	100	0.0144
---	----	-----	--------

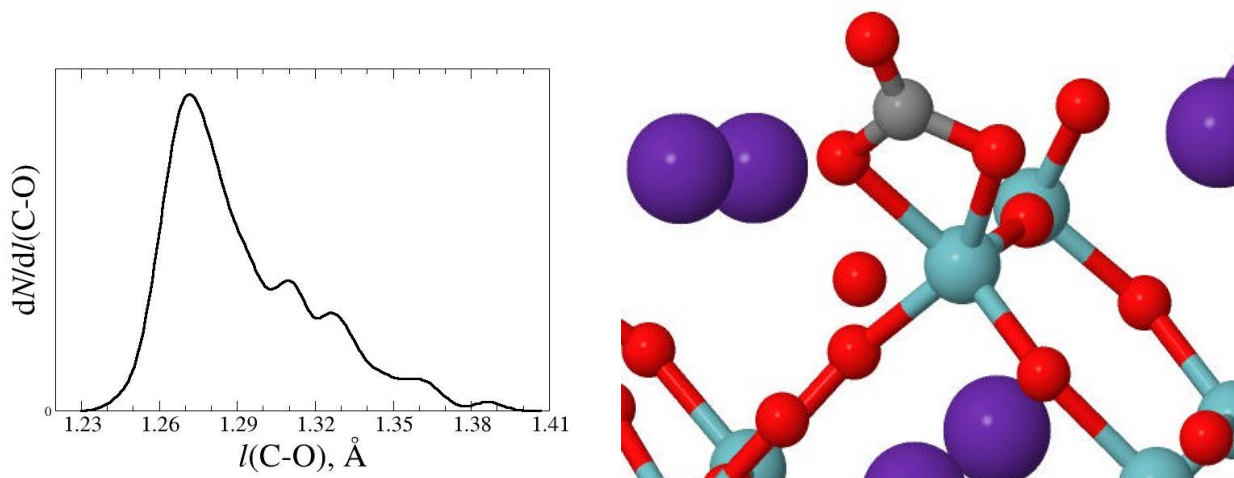


Figure S3. (left) Density of samples with respect to larger of the two C-O bond lengths $l(\text{C-O})$. Gaussian smearing $\sigma = 5 \cdot 10^{-3} \text{ \AA}$ was used to construct the density of samples. (right) Typical CO_2 adsorption structure from the subgroup with larger $l(\text{C-O})$. Color scheme: gray C, red O, cyan Nb, violet Rb.

References

1. Blum, V.; Gehrke, R.; Hanke, F.; Havu, P.; Havu, V.; Ren, X.; Reuter, K.; Scheffler, M. Ab initio molecular simulations with numeric atom-centered orbitals. *Comput. Phys. Comm.*, **2009**, *180*, 2175-2196.
2. J.P. Perdew, K. Burke, and M. Ernzerhof. Generalized gradient approximation made simple. *Phys. Rev. Lett.*, **1997**, *77*, 3865-3868.
3. J.P. Perdew, A. Ruzsinszky, G.I. Csonka, O.A. Vydrov, G.E. Scuseria, L.A. Constantin, X. Zhou, K. Burke. Restoring the density-gradient expansion for exchange in solids and surfaces. *Phys. Rev. Lett.*, **2008**, *100*, 136406.
4. D.M. Ceperley, B.J. Alder. Ground state of the electron gas by a stochastic method. *Phys. Rev. Lett.*, **1980**, *45*, 566-569.
5. B. Hammer, L.B. Hansen, and J.K. Nørskov. Improved adsorption energetics within density-functional theory using revised Perdew-Burke-Ernzerhof functionals. *Phys. Rev. B*, **1999**, *59*, 7413-7421.
6. D.W. Blaylock, T. Ogura, W.H. Green, G.J.O. Beran. Computational investigation of thermochemistry and kinetics of steam methane reforming on Ni(111) under realistic conditions. *J. Phys. Chem. C*, **2009**, *113*, 4898-4908.
7. A.A. Peterson, F. Abild-Pedersen, F. Studt, J. Rossmeisl, J.K. Nørskov. How copper catalyzes the electroreduction of carbon dioxide into hydrocarbon fuels. *Energy Environ. Sci.*, **2010**, *3*, 1311-1315.
8. A. Tkatchenko, M. Scheffler. Accurate molecular van der Waals interactions from ground-state electron density and free-atom reference data. *Phys. Rev. Lett.*, **2009**, *102*, 073005.
9. J. Neugebauer, M. Scheffler. Adsorbate-substrate and adsorbate-adsorbate interactions of Na and K adlayers on Al(111). *Phys. Rev. B*, **1992**, *46*, 16067-16080.

10. B.H. Solis, Y. Cui, X. Weng, J. Seifert, S. Schauer mann, J. Sauer, S. Shaikhutdinov, H.-J. Freund. Initial stages of CO₂ adsorption on CaO: a combined experimental and computational study. *Phys. Chem. Chem. Phys.*, **2017**, *19*, 4231-4242.
11. Y. Wang, R. Kováčik, B. Meyer, K. Kotsis, D. Stodt, V. Staemmler, H. Qiu, F. Traeger, D. Langenberg, M. Muhler, C. Wöll. CO₂ activation by ZnO through the formation of an unusual tridentate surface carbonate. *Angew. Chem. Int. Ed.* **2007**, *46*, 5624–5627.
12. X. Xia, J. Strunk, W. Busser, R. Naumann d'Alnoncourt, M. Muhler. Probing the surface heterogeneity of polycrystalline zinc oxide by static adsorption microcalorimetry. 1. The influence of the thermal pretreatment on the adsorption of carbon dioxide. *J. Phys. Chem. C*, **2008**, *112*, 10938–10942.
13. T. Bučko, S. Lebegue, J.G. Angyan, J. Hafner. Extending the applicability of the Tkatchenko-Scheffler dispersion correction via iterative Hirshfeld partitioning. *J. Chem. Phys.*, **2014**, *141*, 034114.
14. D. Meixner, D. Arthur, S. George. Kinetics of desorption, adsorption, and surface diffusion of CO₂ on MgO(100). *Surf. Sci.*, **1992**, *261*, 141–154.
15. A. Mazheika, S.V. Levchenko. Ni Substitutional Defects in bulk and at the (001) surface of MgO from first-principles calculations. *J. Phys. Chem. C*, **2016**, *120*, 26934–26944.
16. <http://nomad-repository.eu/>
17. V. Vapnik, A. Chervonenkis, Theory of pattern recognition, **1974**. C. Cortes, V. Vapnik. Support-vector networks. *Machine Learning*. **1995**, *20*, 273-297.
18. L.M. Ghiringhelli, J. Vybiral, E. Ahmetcik, R. Ouyang, S. V. Levchenko, C. Draxl, M. Scheffler. Learning physical descriptors for materials science by compressed sensing. *New J. Phys.*, **2017**, *19*, 023017.
19. R. Ouyang, S. Curtarolo, E. Ahmetcik, M. Scheffler, L.M. Ghiringhelli. SISSO: A compressed-sensing method for identifying the best low-dimensional descriptor in an immensity of offered candidates. *Phys. Rev. M*, **2018**, *2*, 083802.
20. A. Tkatchenko, R.A. DiStasio, R. Car, M. Scheffler. Accurate and efficient method for